Calcium Release Flux Underlying Ca^{2+} Sparks of Frog Skeletal Muscle

Eduardo Ríos,* Michael D. Stern,‡ Adom González, Gonzalo Pizarro,§ and Natalia Shirokova*

From the *Department of Molecular Biophysics and Physiology, Rush University, Chicago, Illinois 60612; ‡Laboratory of Cardiovascular Science, Gerontology Research Center, National Institute on Aging, National Institutes of Health, Baltimore, Maryland 21224; and §Departamento de Biofísica, Facultad de Medicina, Universidad de la República, G. Flores 2125, Montevideo, Uruguay

abstract An algorithm for the calculation of Ca^{2+} release flux underlying Ca^{2+} sparks (Blatter, L.A., J. Hüser, and E. Ríos. 1997. *Proc. Natl. Acad. Sci. USA.* 94:4176–4181) was modified and applied to sparks obtained by confocal microscopy in single frog skeletal muscle fibers, which were voltage clamped in a two-Vaseline gap chamber or permeabilized and immersed in fluo-3–containing internal solution. The performance of the algorithm was characterized on sparks obtained by simulation of fluorescence due to release of Ca^{2+} from a spherical source, in a homogeneous three-dimensional space that contained components representing cytoplasmic molecules and Ca^{2+} removal processes. Total release current, as well as source diameter and noise level, was varied in the simulations. Derived release flux or current, calculated by volume integration of the derived flux density, estimated quite closely the current used in the simulation, while full width at half magnitude of the derived release flux was a good monitor of source size only at diameters >0.7 μm. On an average of 157 sparks of amplitude >2 U resting fluorescence, located automatically in a representative voltage clamp experiment, the algorithm reported a release current of 16.9 pA, coming from a source of 0.5 μm, with an open time of 6.3 ms. Fewer sparks were obtained in permeabilized fibers, so that the algorithm had to be applied to individual sparks or averages of few events, which degraded its performance in comparable tests. The average current reported for 19 large sparks obtained in permeabilized fibers was 14.4 pA. A minimum estimate, derived from the rate of change of dye-bound Ca^{2+} concentration, was 8 pA. Such a current would require simultaneous opening of between 8 and 60 release channels with unitary Ca^{2+} currents of the level recorded in bilayer experiments. Real sparks differ from simulated ones mainly in having greater width. Correspondingly, the algorithm reported greater spatial extent of the source for real sparks. This may again indicate a multichannel origin of sparks, or could reflect limitations in spatial resolution.

key words: sarcoplasmic reticulum • excitation–contraction coupling • confocal microscopy • computer algorithm

introduction

Excitation–contraction coupling in striated muscle takes place by the release of stored calcium in response to depolarization of the sarcolemma, via ryanodine receptor channels of the sarcoplasmic reticulum. When studied in frog skeletal muscle by confocal microscopic imaging of the fluorescence of fluo-3, this release is seen to occur largely in the form of discrete events, first described in cardiac muscle (Cheng et al., 1993) and termed Ca^{2+} sparks. A continuous form of release, not constituted by resolvable discrete events, is of comparatively minor magnitude in the frog, where it may have an important mechanistic role (Shirokova and Ríos, 1997), and it is the sole component seen in adult rat muscle under voltage clamp (Shirokova et al., 1998). It is still not clear whether the sparks of cardiac and skeletal muscle are the result of opening of individual channels or of concerted openings of channel clusters (Cannell and Soeller, 1999; Schneider, 1999; Shirokova et al., 1998). One of the approaches that could help elucidate this question is to determine the flux or current of Ca^{2+} release underlying sparks. Blatter et al. (1997) adapted release calculation methods that had been developed earlier for signals from macroscopic cell segments ("whole cell methods"; Baylor et al., 1983; Melzer et al., 1984, 1987) and applied them to sparks of cardiac myocytes. In the present paper, we apply this method to sparks recorded in frog skeletal muscle under different conditions. Taking a clue from earlier work with whole cell methods (Melzer et al., 1984, 1987; Schneider et al., 1987), we first tested the technique by simulating sparks (as the result of release from spatially and temporally discrete sources), and then applying the release calculation algorithm to the simulated sparks.

By this combination of forward (i.e., simulation of sparks) and backward calculations (the release algorithm), we found that the method recovers adequately the current of release flux. We also uncovered limita-

Dr. Shirokova's permanent address is A.A. Bogomoletz Institute of Physiology, Bogomoletz St. 4, Kiev, Ukraine.

Address correspondence to Eduardo Ríos, Department of Molecular Biophysics and Physiology, Rush University, 1750 W. Harrison Street, Chicago, IL 60612. Fax: 312-942-8711; E-mail: erios@rush.edu

tions of the method, manifested in errors in the determination of release magnitude, source diameter, or release flux duration, and established circumstances that make these errors greater or reduce them.

When the release calculation algorithm was applied to sparks obtained experimentally in skeletal muscle under different conditions, the resulting flux was large by comparison with Ca^{2+} flux measured through single channels in bilayers under what are thought to be near-physiological conditions (Mejía-Alvarez et al., 1998), suggesting a multichannel origin for sparks.

methods

Determination of the Point Spread Function

The point spread function (PSF),[1] a function $P(x,y,z)$, was determined generally following procedures discussed by Agard et al. (1989). We used fluorescent beads of subresolution size (0.1 μm diameter; Molecular Probes, Inc.) with the laser scanner and microscope (MRC 1000; Bio-Rad Laboratories) operating under the same conditions (highest scanning speed, zoom factor set to one spot per 0.1425 μm, iris diameter 2 mm) as in the experiments, and the same objective (C-apochromat 40×, 1.2 N.A., water immersion lens; Carl Zeiss, Inc.), filters, and glass (#0 coverslip, with the correction collar of the objective set for minimum glass thickness). Before the determination of the PSF, the alignment of the system was optimized following the manufacturer's recommended procedure. Two techniques were used to immobilize the beads. In one, the bead-containing suspension was painted and dried on a glass slide, antifade solution and a coverslip were added, and the beads were then imaged through the coverslip. In the other, the beads were immobilized in an aqueous 4% agar gel. The second method gave a slightly more symmetrical PSF. The PSF was determined by serial optical sections (or xy scans) at different axial (z axis) levels. The z axis level was determined by the stepping motor acting on the vertical nosepiece focusing of the microscope (Axiovert 100-TV; Carl Zeiss, Inc.), which in turn was calibrated by focusing on an object of known dimensions. The three-dimensional array of fluorescence intensities thus obtained was simplified (under the assumption of cylindric symmetry) to a two-dimensional array. For this, the average per pixel was calculated at each value of z, in annular bins in the xy plane, at 0.1425-μm intervals of the radial distance from the center [$r = \sqrt{(x^2 + y^2)}$].

The fluorescence averaged in this way is represented versus r and z in Fig. 1 A. The dependence could be fitted as the product of two gaussians: $P = G(r)\,H(z)$, where $G = k \exp[-0.5\,(r/\sigma_{xy})^2]$, $H = \exp[-0.5(z/\sigma_z)^2]$, $\sigma_{xy} = 0.20$ μm, and $\sigma_z = 0.614$ μm. The two-gaussian description, which is used later in the analysis, is documented in B and C. Fig. 1 B contains data as a function of the axial coordinate *z*. The fluorescence values represented are averages within each section, over a 0.1425-μm circle centered on the $x = 0$, $y = 0$ line (●), or in a ring region $0.285 < r < 0.4275$ μm (○). The lines are best fit gaussians with $\sigma = 0.608$ and 0.736 μm, respectively, indicating some deviation from the product of gaussians at high values of *r*. In Fig. 1 C, the fluorescence is represented as a function of distance *r* at constant *z*. The three sets of data are from the central section ($|z| < 0.18$ μm; ●), an intermediate region ($0.18 < |z| < 0.54$ μm; dotted symbols), and an outlying region ($0.72 < |z| < 0.98$ μm; ○). The best fit gaussians shown have very similar spread ($\sigma = 0.196$, 0.2, and 0.207 μm, respectively). In the analysis of data, we neglect the deviations and approximate the PSF as a product of a gaussian function of *r*, with $\sigma_{xy} = 0.2$ μm (corresponding to a full width at half magnitude [FWHM] of 0.47 μm) and a gaussian function of *z*, with $\sigma_z = 0.615$ μm (FWHM of 1.44 μm). Similar values were obtained with a second C-apochromat 1.2 N.A. objective in our microscope, and with either objective in a LSM 410 (Carl Zeiss, Inc.) confocal scanner.

The *xy* or focal spread measured was close to the expected value for this objective and wavelengths of excitation and emission (e.g., Sako et al., 1997), but the axial spread was worse than expected. To rule out trivial errors in scanner alignment, we carried out extensive comparisons of axial PSFs, using the front surface reflection method (which gives less spread than subresolution beads; Wilson, 1995) and different objectives, after aligning the system for the objective in use. With the C-apochromat, the $FWHM_z$ was 1.50 μm with a 2.0-mm iris and 1.15 μm using a 0.7-mm iris. With the same technique, a plan-apochromat, 63×, 1.4 N.A., oil immersion objective (Carl Zeiss, Inc.) gave a $FWHM_z$ of 0.98 μm with a 2-mm iris, and 0.63 μm using the 0.7-mm iris. An 60×, 1.4 N.A., oil objective (Olympus Corp.) gave slightly higher resolution in the focal plane and approximately the same in the axial direction as the plan-apochromat. These results indicate that the wider axial spread is a characteristic of the C-apochromat objective and is increased substantially by the larger iris. Even though this seems to imply that the oil immersion objective is better for recording sparks, the spark morphology did not change significantly with the two objectives. On the other hand, the water immersion objective has three advantages, it collects ~2.5× greater fluorescence intensity at comparable magnification, this fluorescence intensity is nearly independent of vertical position of the focal plane within the fluorescent object or solution, and its working distance is substantially greater. For these reasons, it was used in most of the experiments reported here.

Imaging of Fluorescence Sparks

Imaging of fluorescence sparks was carried out in segments of singly dissected semitendinosus muscle fibers of Rana pipiens (which were anesthetized in a 15% ethanol solution, and then killed by pithing), using two conventional techniques for eliciting sparks. In one, fiber segments were voltage clamped in a two-vaseline gap chamber, while their cytoplasmic medium was equilibrated with an "internal" solution containing (mM): 125 Cs-glutamate, 10 Cs-HEPES, 0.5 $MgCl_2$, 1 EGTA, nominal [Ca^{2+}] set to 100 nM, 0.1 fluo-3, 5 creatine-phosphate, 5 Mg-ATP, 5 glucose, pH 7.0. The "external" solution in the middle pool of the chamber contained (mM): 131.5 tetraethylammonium (TEA)–methanesulfonate, 10 TEA-HEPES, 10 Ca-methanesulfonate, 10^{-6} g/liter tetrodotoxin. In this case, sparks were elicited by voltage clamp depolarization to low voltages (between −70 and −50 mV). In the other technique, similar to that described by Lacampagne et al. (1998), the fiber segment was mechanically fixed to the coverslip bottom of a single compartment chamber. Its membrane was permeabilized by several large cuts, at distances of 100–150 μm, or by brief exposure to an internal solution with 0.01% saponin, and immersed in internal solution with fluo-3. Because one of the purposes of using the permeabilized fiber was to reach higher dye concentrations more rapidly inside the cells, the internal solution in this case contained 0.2 mM fluo-3. To elicit sparks, the internal solution contained lower nominal [Mg^{2+}] (0.15–0.3 mM; Lacampagne et al., 1998), and total ATP was increased for a nominal [Mg ATP] of 5 mM. All solutions were titrated to pH 7.0. The experiments were carried out at 17°C.

[1]*Abbreviations used in this paper:* FDHM, full duration at half magnitude; FWHM, full width at half magnitude; PSF, point spread function; SR, sarcoplasmic reticulum.

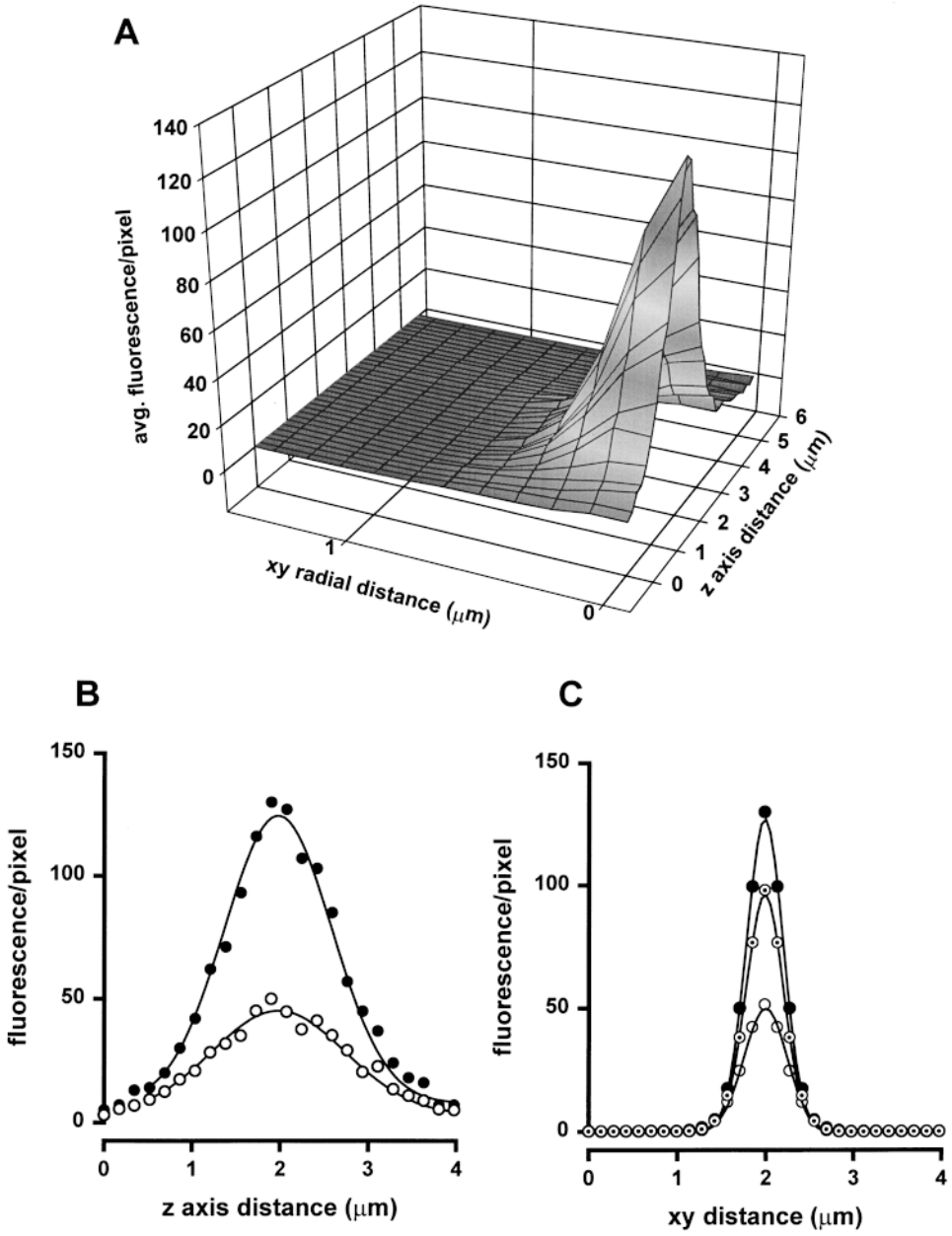

Figure 1. The system's PSF. (A) Fluorescence intensity in *xy* sections of the image of a 0.1 μm bead, plotted as a function of distance in the plane of the section and value of the axial variable *z*. For each *xy* section (or discrete *z* value) data were reduced to a function of the radial distance to the center of the bead ($r = \sqrt{x^2 + y^2}$) by averaging fluorescence in concentric rings of increasing radius. (B) Average fluorescence per pixel as a function of axial distance, at the center of the bead ($r < 0.14$, ●) and in the ring between 0.285 and 0.428 μm (○). The continuous curves are gaussian fits with parameters given in the text. (C) fluorescence versus *r*, for three ranges of *z*, and the corresponding gaussian fits (ranges and parameter values given in text).

Ca^{2+} sparks were imaged in line scan mode. Images are formed by juxtaposition of 768 line scans of 512 pixels obtained at 2-ms intervals and stored as arrays $F(x_j,t_i)$, [sometimes referred to as $F(x,t)$], where j and i are integers varying between 1 and 768 and 1 and 512, respectively. Experimental images are presented normalized to the resting fluorescence $F_0(x)$, calculated by averaging $F(x,t)$ over time. In the voltage-clamp experiments, this averaging is restricted to the interval before the depolarizing pulse. In the experiments with permeabilized fibers, it is done after removing the spark regions located automatically by a simple amplitude criterion applied to a filtered version of the image (Cheng et al., 1998).

Analysis of Fluorescence Images

Once the events were located, all subsequent analysis was carried out on subsets of the line scan, 45 × 45 arrays, centered at the peak of the located spark. Four morphological parameters were determined first: amplitude (*a*) full width at half magnitude, full duration at half magnitude (FDHM), and rise time. *a* was determined as the difference between the peak value of the normalized fluorescence and its baseline value at the same spatial position immediately before the event (the average of 10 values between 40 and 20 ms before the peak). FWHM was determined on the spatial distribution of fluorescence at the time of maximum change. FDHM was determined on the time dependence at the spark center. Rise time as the interval between time to 10% increase from pre-event baseline and time to peak, determined on a spline interpolate of the time-dependent fluorescence, averaged over three spatial pixels at the center of the spark. Even though the event locator uses filtration steps, the morphometric measurements were carried out on the unfiltered image, normalized as described. In some cases, averages were made of the events located automatically.

Fluorescence line scan images were analyzed to derive $[Ca^{2+}](x,t)$ and release flux, following a procedure modified

from that of Blatter et al. (1997). When the dye concentration is low, so that autofiltration can be neglected, and the dye is in equilibrium with Ca^{2+}, fluorescence is

$$F = M\,B'_{\min}([\mathrm{dye}] + R'[\mathrm{dyeCa}^{2+}])$$
$$= M\,B'_{\min}\frac{K'_d + R'[\mathrm{Ca}^{2+}]}{K'_d + [\mathrm{Ca}^{2+}]}dye_T, \quad (1)$$

where K'_d is the dye's dissociation constant in the cytoplasmic medium, R' is the ratio between the fluorescence of Ca^{2+}-bound and free dye, M is the adjustable gain of the scanner, $B'_{\min}$ is a constant and dye_T is total dye concentration. (As follows from Eq. 1, the minimum and maximum fluorescence were derived as $F_{\min} = B'_{\min} M\, dye_T$ and $F_{\max} = R'\,F_{\min}$). The parameters of fluo-3 were given values within the range estimated by Harkins et al. (1993) for the cytoplasmic medium. Specifically, $K'_d = 1.03$ μM and $R' = 100$.

Dye_T, a function of position x along the scanned line, was calculated replacing F in Eq. 1 by $F_0(x)$, the fluorescence averaged over time during the periods of rest before the sparks of interest (or voltage pulse), and assuming the resting concentration $[Ca^{2+}]_0$ to be equal to the concentration in the internal solution, 100 nM.

When $[Ca^{2+}]_0$ is much lower than K'_d (for instance at 100 nM), a simplification applies

$$F = B'_{\max}\frac{[\mathrm{Ca}^{2+}]}{K'_d}M\,dye_T,; \quad (2)$$

where $B'_{\max} = R'\,B'_{\min}$. For the calibration situation Eq. 2 applies, with $B_{\max}$ and K_d substituted for the corresponding values inside the cell. From this calibration, an approximate formula follows for the dye concentration: $dye_T/100\ \mu M = (F_0/F_{100})\ ([Ca^{2+}]_0/100\ nM)\ (K'_d/K_d)\ (B_{\max}/B'_{\max})$, where F_{100} is the fluorescence in cuvette at 100 μM $[Ca^{2+}]$ and 100 μM dye_T. K_d is 0.48 μM in our cuvette calibrations. Assuming that the resting $[Ca^{2+}]$ is equal to 100 nM and that $B_{\max}/B'_{\max} \approx 1$ (Harkins et al., 1993), the equation simplifies further to $dye_T \approx 2 \times 100\ \mu M\ (F_0/F_{100})$. Because F_0 is in general a function of x, dye_T is also a function of x. If, instead of 1.03 μM, we used the upper estimate of Harkins et al. (1993) for K'_d, 2.53 μM, the estimate of dye_T would increase by a factor of ~2.5. In this sense, we used a low estimate of dye_T.

When $[Ca^{2+}]$ is changing steeply in space and time, we evaluate it as that needed to produce the observed distribution of *dye*:Ca^{2+}, the concentration of which is proportional to the observed changes in fluorescence. Specifically, $[dye{:}Ca^{2+}]$ was derived from the spatially resolved fluorescence $F(x,t)$, using $[dye{:}Ca^{2+}](x,t) = \mathrm{dye}_T(x)\ [F(x,t) - F_{\min}(x)]/[F_{\max}(x) - F_{min}(x)]$. Then $[Ca^{2+}](x,t)$ was obtained numerically solving the diffusion–reaction equation that governs the evolution of $[dye{:}Ca^{2+}]$:

$$\frac{\partial[dye{:}\mathrm{Ca}^{2+}](x,t)}{\partial t} = [dye](x,t)[\mathrm{Ca}^{2+}](x,t)k_{on}$$
$$-[dye{:}\mathrm{Ca}^{2+}](x,t)k_{off} + D_{\mathrm{dyeCa}}\Delta[dye{:}\mathrm{Ca}^{2+}](x,t), \quad (3)$$

where k_{on} and k_{off} are the rate constants of the fluo-3:Ca^{2+} reaction, D_{dyeCa} is the diffusion coefficient, and Δ is the laplacian operator ($\partial^2/\partial x^2 + \partial^2/\partial y^2 + \partial^2/\partial z^2$). The line scan only provides the partial derivative in the x direction. Blatter et al. (1997) used $3\,\partial^2/\partial x^2$ as an approximation to Δ. M. Cannell (University of Auckland, New Zealand, personal communication) suggested assuming that the fluorescence increase is spherically symmetric, a function of time and the distance (ρ) to its center. In that case, the dependence of F with x gives all the information needed to calculate the laplacian correctly, as $\partial^2/\partial x^2 + 2\,(\partial/\partial x)/x$. This approximation does not work when the sources of release are spatially complex (as in Blatter et al., 1997), but seems better in the present case, when there are few evidences of spatial complexity. The approximation has some drawbacks: the first is that the operation applied to finite functions F leads to a singularity at $x = 0$. In actual work, this is avoided by using interpolated arrays that do not include $x = 0$. Still, at the smallest x values, the operation increases local noise greatly, which may result in the appearance of spurious sources when working on noisy data. Additionally, the source may not be spheric if it is constituted by multiple channels. An estimation of the errors expected if the source was not spheric is presented in results.

Calculation of Release Flux

Calculation of release flux was done as described by Blatter et al. (1997). The flux density of the source, represented as $\dot{R}$, satisfies the equation

$$\dot{R} = \partial[\mathrm{Ca}^{2+}]/\partial t - D_{\mathrm{Ca}}\Delta[\mathrm{Ca}^{2+}]$$
$$+\partial[dye{:}\mathrm{Ca}^{2+}]/\partial t - D_{dye:\mathrm{Ca}}\Delta[dye{:}\mathrm{Ca}^{2+}] + \partial rem/(\partial t), \quad (4)$$

where D_{Ca} and $D_{dye:\mathrm{Ca}}$ are the diffusion coefficients of Ca^{2+} and its complex with the dye. $\partial rem/\partial t$ is a sum of terms of the form

$$\partial[b{:}\mathrm{Ca}^{2+}]/\partial t - D_{b:\mathrm{Ca}}\Delta[b{:}\mathrm{Ca}^{2+}] \quad (5)$$

for each intrinsic buffer b of the cell (parvalbumin, ATP, nondiffusible sites in troponin and the sarcoplasmic reticulum, SR), plus the flux density of sinks (a positive function of space and time). Buffers are assumed to be homogeneously distributed.

The terms of Eq. 5 are calculated from the function $[Ca^{2+}](x,t)$, solving for $[b{:}Ca^{2+}]$ the diffusion–reaction equation of form 3 for the corresponding buffer. In general, this requires simultaneously solving an equation for the free buffer (see for instance Eqs. 1–4 in Ríos and Stern, 1997). This is avoided in the present calculations assuming that the free buffer and its Ca^{2+} complex have the same diffusion coefficient, or equivalently that total buffer concentration is constant everywhere. In the case of parvalbumin and ATP, buffers that react with both Ca^{2+} and Mg^{2+}, diffusion–reaction equations of form 3 still apply, but $[b{:}Ca^{2+}]$ is in both cases equal to $[b]_T - [b] - [b{:}Mg^{2+}]$ (where $[b]_T$ is the total concentration of buffer), and $[b{:}Mg^{2+}]$, a function of space and time, is calculated from its own diffusion reaction equation

$$\frac{\partial[b{:}\mathrm{Mg}^{2+}](x,t)}{\partial t} = [b](x,t)[\mathrm{Mg}^{2+}]k_{on}$$
$$-[b{:}\mathrm{Mg}^{2+}](x,t)k_{off} + D_b\Delta[b{:}\mathrm{Mg}^{2+}](x,t), \quad (6)$$

assuming $[Mg^{2+}]$ to be constant.

Parameter values are given in Table I. The SR pump contribution to removal was proportional to the fractional occupancy of pump sites of dissociation constant 1 μM, with maximum (saturation) pump rate given in the table. An exploration of the effects of changing the assumed values of the parameters is presented later.

Numerical processing of data was done in the IDL environment (Research Systems Inc.). When specifically stated, the records of fluorescence were first subjected to three-point smoothing (replacing each value by the "boxcar" average of the three-element–wide array that surrounds it). Differentiation with respect to spatial coordinates was carried out by convolution with a 17-element Kaiser window kernel, with a corner frequency of either 2.45 or 1.75 μm^{-1} (Hamming, 1989). Smoothing and the heavier filtering differentiator were used when processing individual sparks, but not when analyzing averages.

TABLE I

Values of Parameters Used by the Release Flux Algorithm

Parameter	Value	
Fluo-3:Ca on rate	3.2×10^7 M^{-1} s^{-1}	Harkins et al. (1993)
Fluo-3 dissociation constant	1.03 μM	Harkins et al. (1993)
EGTA:Ca on rate	0.2×10^7 M^{-1} s^{-1}	Smith et al. (1984)
EGTA dissociation constant	1 μM	Smith et al.(1984)
Trop:Ca on rate	5.7×10^6 M^{-1} s^{-1}	Baylor et al. (1983), model 3
Trop:Ca off rate	11.4 s^{-1}	Baylor et al. (1983), model 3
ATP:Ca on rate	1.5×10^6 M^{-1} s^{-1}	Baylor and Hollingworth (1998)
ATP:Ca off rate	3×10^4 s^{-1}	Baylor and Hollingworth (1998)
ATP:Mg on rate	1.5×10^6 M^{-1} s^{-1}	Baylor and Hollingworth (1998)
ATP:Mg off rate	195 s^{-1}	Baylor and Hollingworth (1998)
Parv:Ca on rate	1.25×10^8 M^{-1} s^{-1}	Baylor et al. (1983), model 3
Parv:Ca off rate	0.5 s^{-1}	Baylor et al. (1983), model 3
Parv:Mg on rate	3.3×10^4 M^{-1} s^{-1}	Baylor et al. (1983), model 3
Parv:Mg off rate	3 s^{-1}	Baylor et al. (1983), model 3
Maximum pump rate	9.8 mM s^{-1}*	
[Parvalbumin]	1 mM	Baylor et al. (1983), model 3
[Pump sites]	0.2 mM	Baylor et al. (1983), model 3
[EGTA]	1 mM	Value in solution
[ATP]	5 mM	Value in solution
D_{Ca}	3.5×10^{-6} cm^2 s^{-1}	Kushmerick and Podolsky (1969)
D_{dye}	2×10^{-7} cm^2 s^{-1}	Harkins et al. (1993)
D_{ATP}	1.4×10^{-6} cm^2 s^{-1}	Baylor and Hollingworth (1998)
D_{parv}	2.6×10^{-7} cm^2 s^{-1}‡	
D_{EGTA}	3.6×10^{-7} cm^2 s^{-1}	Pizarro et al. (1991)§

Parv, parvalbumin. Trop, troponin. $[Ca^{2+}]$ was 0.1 μM unless noted otherwise. $[Mg^{2+}]$ was 0.61 or 0.15 mM, depending on the experiment. *A value that fits global calcium transients when other parameters of removal had the values listed. ‡Based on Pechère et al. (1973). §1.7×10^{-6} cm^2 s^{-1} (Baylor et al., 1983) was used in other computations with [EGTA] = 1 mM without significant changes.

Simulations (Calculations of Fluorescence Sparks)

Reaction–diffusion equations (Ríos and Stern, 1997) were written to describe the movements of Ca^{2+}, Ca^{2+} -bound, and Ca^{2+}-free fluo-3 in the presence of an isotropic myoplasm containing endogenous buffers (troponin, SR pump, parvalbumin, ATP) and EGTA. EGTA, ATP, and parvalbumin species were treated as diffusible. In most of the simulations illustrated, the spark was modeled as the fluorescence increase resulting from a 5-ms square wave release of calcium (of current intensity that varied between 0.1 and 25 pA) deposited uniformly into a sphere (the diameter of which varied between 100 and 1,500 nm). Additional simulations were carried out with other time dependencies or with cylindric sources. The reaction–diffusion equations were solved by the Galerkin finite element method with adaptive gridding, using the program PDEASE (Macsyma Inc.). The resulting function of spatial position is spherically symmetric (a function, $f(\rho)$, of radial distance to the center of the release sphere), and was generated as a two-dimensional array for suitable values of ρ and time. To make it comparable with the experimental results, these arrays were spaced at increments of 0.15 μm and 2 ms.

The simulation approach, including the assumption of a homogeneous medium, isotropic for removal and diffusion, was similar to that of Smith et al. (1998), who did it for a specifically cardiac removal system. The resulting sparks were of smaller normalized amplitude for the same release current in the present work, because we assumed a briefer release in a medium that included higher [fluo-3], diffusible buffers (EGTA, ATP, and parvalbumin) and a higher concentration of troponin. Additionally, we used a broader PSF when blurring the simulated sparks.

Blurring and Deblurring

Blurring, the effect of the limited resolution of the microscope when imaging fluorescence sparks, was simulated assuming a point spread function similar to that determined experimentally. Let F represent the detected fluorescence, or fluorescence in image space. The object fluorescence, $f(x,y,z)$, is always assumed to be a spherically symmetric function (of radial distance to the center of the spark). In general (Agard et al., 1989), the image of this object will be the convolution of f with the PSF P, which for a given time results in a function of three space coordinates.

$$F(X, Y, Z) = \iiint f(x, y, z)P(x - X, y - Y, z - Z)dx\ dy\ dz. \quad (7)$$

Because in all cases we processed or simulated line scans, we only concerned ourselves with the dependence of F on X. Additionally, we only processed sparks assumed to be centered on the scanning line. Therefore, the function F above only had to be evaluated at $Y = 0$ and $Z = 0$. Representing $F(X,0,0)$ as $F(X)$, Eq. 7 simplifies to

$$F(X) = \iiint f(x, y, z)P(x + -X, y, z)dx\ dy\ dz. \quad (8)$$

We further simplified Eq. 8 because the PSF, as shown in results, is approximately separable as the product of two gaussian functions: $G(x,y) = \exp\{-[(x^2 + y^2)/2\sigma_{xy}^2]\}/2\pi\sigma_{xy}^2$, a function of the radial distance to the center of the scanned spot in the focal plane, and $H(z) = \exp\{-[(z^2)/2\sigma_z^2]\}/\sigma_z\sqrt{2\pi}$, a function of the axial distance to the focal plane, in the z axis direction. The simulated fluorescence spark is spherically symmetrical $[f_\rho(\rho)]$. It is well fitted by a gaussian function of polar radius (as shown with an example in discussion), namely

$$\begin{aligned} &f_p(0)\exp[-(x^2 + y^2 + z^2)/2\sigma^2] \\ &= f_p(0)\exp(-x^2/2\sigma^2)\exp(-y^2/2\sigma^2)\exp(-z^2/2\sigma^2) \\ &= f_p(0)\ g(x)\ g(y)\ g(z). \end{aligned} \quad (9)$$

With these approximations, the blurred function $F(X)$, Eq. 8, simplifies to:

$$F(X) = f_\rho(0)\int g(x)G(x - X)\int g(y)G(y)dy\int g(z)H(z)dz, \quad (10)$$

where $G(x - X) \equiv G(x - X, 0)$ and $G(y) \equiv G(0, y)$.

This is done for every point in time and presented to the release calculation algorithm as a line scan image of a spark. A simulated spark before and after blurring is illustrated (see Fig. 2, A and B).

The analysis of fluorescence sparks, real or simulated, starts with a deblurring step to recover the object spark. We assume, in agreement with our analysis of simulated sparks, that the object spark can be put as the spherically symmetric function $f_\rho(0)$ $g(x)g(y)g(z)$. The form of the function g is deduced deriving from Eq. 10 the expression

$$f_\rho(0)\int g(x)G(x-X)dx = \frac{F(X)}{JL}, \quad (11)$$

where $F(X)$ is the line scan image, and J and L are constants, the integrals over y and z in Eq. 10. Therefore, $g(x)$ is the deconvolution of F and the spatial spread G, scaled so that $g(0) = 1$. Evaluating Eq. 11 at $X = 0$, it follows that $f_\rho(0) = F(0)/J^2L$. In more intuitive terms, deblurring changes the spatial shape of the spark from F to g, making it sharper, and rescales it by the factor $1/J^2L$, which "undoes" the three-dimensional averaging and consequent loss in amplitude, due to the spread of the microscope. J and L quantify these averaging effects and are therefore smaller than 1. The final expression of the deblurred line scan is $F(0)g(x)/J^2L$, a function that is calculated at every time t_j in the experimental arrays, or at arbitrary increments in simulations.

The deblurring operation is tested in Fig. 2, A and B. The simulated spark before blurring is within 5% of that recovered after successive blurring and deblurring. When applied to noisy data, deblurring may lead to uninterpretably noisy results. In such cases, we used either no or partial deblurring (assuming a sharper PSF). The effects of partial deblurring, evaluated for simulated and experimental data, are illustrated (see Fig. 4).

results

The basic self-consistency of the method is established by first applying it to simulated sparks. Then tests are presented on simulated sparks plus noise, which give a more realistic picture of the method's value and limitations. The algorithm is then applied to experimental sparks. The study ends with a consideration of lower bounds of the release estimate, crucial to evaluate the possibility that a spark may be caused by a single channel.

Tests of the Algorithm on Simulated Sparks

Sparks were simulated as described in methods, as the increase in fluorescence determined by release of Ca^{2+} from a spherical source into a homogeneous medium whose removal properties copied those of the skeletal myoplasm. It includes components with the properties of the most important removal processes in the cell; namely, parvalbumin, troponin, the SR pump, the extrinsic buffer EGTA, which in the experiments analyzed later is present at 1 mM, and ATP, a rapidly diffusing low affinity buffer (Baylor and Hollingworth, 1998). The model parameters had values taken from the literature, listed in Table I. Shown are simulations with a release current of 20 pA and 5-ms duration, originating from a sphere of 0.2-μm radius. These simulated sparks were similar to an average experimental spark shown later. To reproduce the conditions of this average, they were generated assuming a dye concentration of 50 μM.

Simulated sparks were first blurred (according to Eq. 10) with half widths $FWHM_{xy} = 0.4$ μm and $FWHM_z = 1.4$ μm, to produce the effect of detection by the confocal microscope in its usual configuration. The final result of the simulation, with or without blurring, is represented in Fig. 2, A and B, as normalized fluorescence profiles that pass through the maximum, at constant t and x. In thin lines is the spark before blurring ("simulated"). In thick trace is the spark after imaging ("blurred"). It is broader and of approximately half the amplitude of the object spark. The release calculation algorithm starts with a deblurring step (Eq. 11), which seeks to reconstruct the object spark. Its result is represented by the dashed curves ("deblurred"), and is similar to the original simulated spark.

In Fig. 2, C and D, the release flux density used in the simulations is compared with that reported by the release algorithm. The release flux density used in the simulations was calculated as $I/(2F)/v_s$ (where F is the Faraday constant and v_s is the volume of the source, a sphere of radius 0.2 μm) and is represented by the thin trace. The curves in the thick trace represent release flux density calculated by the algorithm ("derived"), in Fig. 2 C as a function of position (x) at the maximum of release, and in D as a function of time at the center of the source.

As seen in both representations, the derived release is a reduced and spread out version of the release used in the simulation. The peak of the derived flux is 1,750 mM/s rather than the theoretical 3,100 mM/s. The full duration at half magnitude, 4.7 ms, is in excellent agreement with release duration. The half width of the derived release is somewhat greater (0.46 μm) than that used in the simulation (0.4 μm). Total release flux was computed by volume integration of the spherically symmetric flux density. Expressed as a current (plotted versus time in Fig. 2 E) and compared with the current of 20 pA used in the simulation. The current initially lags behind the correct value and later overshoots it, but yields a reasonable estimate. This is shown in Fig. 2 F, where the peak of the derived release current is plotted against the simulation current. A good correspondence is found in the range explored, with some evidence of saturation at the high end.

Fig. 2 C illustrates that release typically undershoots, going negative at the edges of the releasing volume. This error is due in part to the use of a wide kernel for spatial differentiation. It is also due to the inherent imprecision of an analysis that samples a continuous physical phenomenon at spatial and temporal frequencies that are comparable with those in the sampled object. Though small in amplitude relative to the positive peak of release, the error becomes proportionally greater when total flux is calculated by integration over the volume of the spark. For this reason, when calculating total flux, the volume integration is stopped at the first negative value of the computed release waveform.

The method was also tested with simulations that specifically violated the assumption of spherical symmetry at the source, in which release originated from a cylinder of 1-μm length and 0.2-μm radius (not shown).

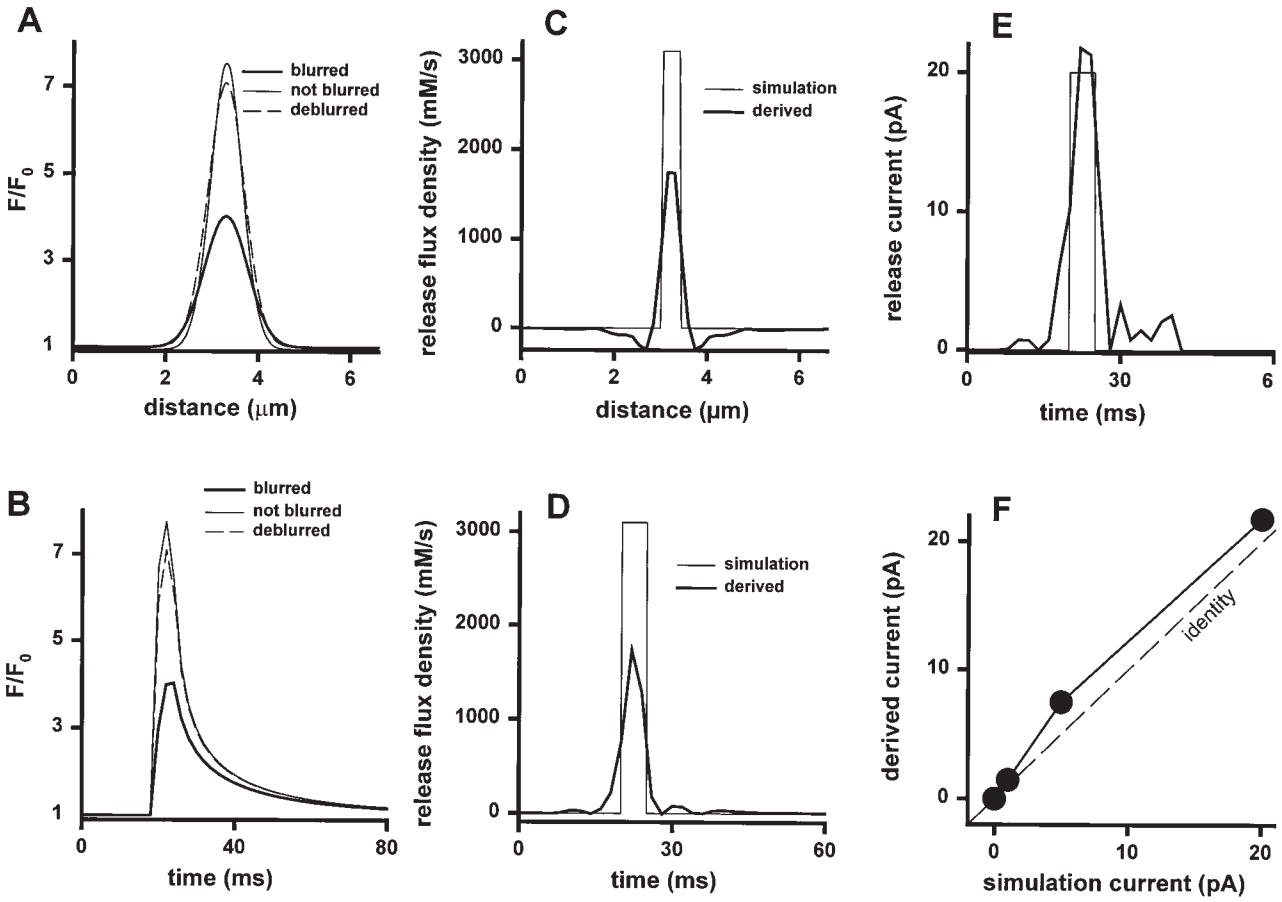

Figure 2. Release analysis of a simulated spark. Fluorescence spark simulated for a source of 0.2-μm radius, 20 pA Ca^{2+} current, active for 5 ms, with a removal system of parameter values listed in Table I, fluo-3 concentration of 50 μM, and $[Mg^{2+}]$ = 610 μM. (A) Spatial profile of the fluorescence (relative to its initial value) at the end of the source open time. (B) Temporal profile at the center of the spark (source current started at time 20 ms). For A and B, the curves in continuous thin line represent the simulation before blurring, the thick line is after blurring (with $FWHM_z$ = 1.4 μm and $FWHM_{xy}$ = 0.4 μm), and the dashed line is after deblurring, the first step in the calculation of release. All simulated sparks shown henceforth include blurring. (C) Spatial dependence of calculated release flux density ("derived," thick line) and flux used in simulation (thin line). (D) Time dependence of flux density at the center of the spark. (E) Volume integral of release flux density, converted to Ca^{2+} current, for the release used in the simulation (thin line) and the detected release (thick line). (F) Peak value of derived release current, plotted versus the source current in different simulations.

The current derived by the algorithm in this case overestimated the simulation current when the simulated spark was scanned along the axis of the cylinder and underestimated it when scanning transversely. The errors, however, were within 50% in either direction.

The conclusion from this section is that the release calculation algorithm is self-consistent—it recovers approximately the input current used in simulations. More realistic tests required adding noise to the simulated sparks.

Performance of the algorithm in the presence of noise. Figs. 3 and 4 illustrate performance of the algorithm in the presence of noise. In Fig. 3, the algorithm operates on (A) the simulated fluorescence spark of Fig. 2 (corresponding to a release current of 20 pA and 5 ms), to which pseudo-random noise has been added, with normal distribution of standard deviation 3 in fluorescence units. Such noise amounts to ~10% of F_0, which is comparable with that of averaged experimental records. The main problem resulting from the presence of noise at this level is that the deblurring correction, which increases the higher frequency components more, may give uninterpretably noisy results. In the example, we used a partial deblurring correction for a less severe microscope spread ($FWHM_z$ = 0.88 instead of 1.4 μm). The consequences of partial deblurring are explored later.

Fig. 3, B and C, plots multidimensionally the resulting release flux waveform; quantitative aspects are in D–F. Due to the partial correction, the resulting release flux is a worse underestimate than in the case of Fig. 2, and the "footprint" of release is wider than the actual source. The half duration of release was 6 ms, and the half width 0.55 μm, or 35% greater than the diameter of the simulation source. The underestimation of flux density and overestimation of spatial width tend to

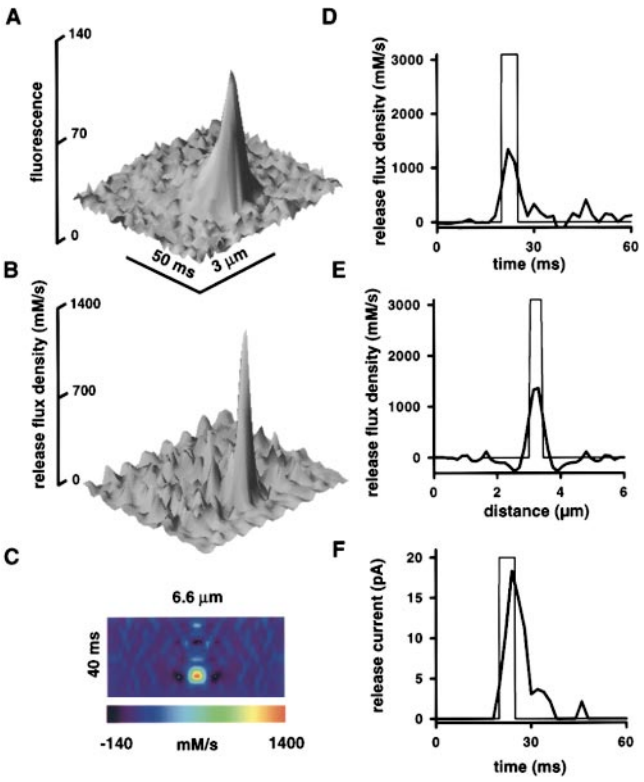

Figure 3. Release analysis of a simulated spark with noise. (A) Fluorescence spark of Fig. 2 (0.2-μm source radius, 20 pA/5 ms Ca^{2+} current, with removal parameters listed in Table I, blurred as described) plus normally distributed noise of SD = three fluorescence units. (B and C) Representations of the release flux derived by the algorithm. (D) Temporal and (E) spatial profiles of the calculated release flux density (thick line) and the flux used to generate the spark (thin line). (F) Derived release current (thick line), and release current used in the simulation (thin line). The application of the algorithm included partial deblurring, with $FWHM_z$ = 0.88 μm and $FWHM_{xy}$ = 0.25 μm (see text for details).

compensate, so that the integrated current peaked at 18.4 pA in the example shown, close to the 20 pA used to generate the spark. In summary, if the noise level prevents application of the deblurring operation, then the release flux density is broadened and more severely underestimated, while the source current is still evaluated fairly well.

Because it was not possible in general to use the full deblurring correction with experimental records, we evaluated in detail the effect of deblurring under different assumptions for the system's PSF. Results are represented in Fig. 4 A, where the peak release current derived for simulations analogous to those in Figs. 2 and 3 is plotted against "deblurring length," the $FWHM_z$ assumed for correction. The values of deblurring length spanned the range from 0 (i.e., no correction), to 1.4 μm ("full correction"). In every case, $FWHM_{xy}$ was equal to $FWH_z/3.5$. (Fig. 4) ● represents simulations without noise and ◆ records with noise (at levels comparable with those in Fig. 3 and an average spark presented later).

It can be seen that increasing the blurring correction increases the estimate of release current, which tends to the correct values as the deblurring length increases. The changes are moderate and vary continuously with deblurring length. When noise is present, the dependence of the parameters on deblurring length changes abruptly at or near 1 μm, indicating that the deblurring correction does not work properly beyond this point (another evidence, not shown, is that the results become variable with each different realization of pseudo-random noise). This test indicates that the algorithm applied with partial deblurring still evaluates source current acceptably, to some extent underestimating it. This issue will be considered further when processing experimental sparks.

Additional tests evaluated the ability of the algorithm to monitor current when spatial aspects of the source were varied. Simulations were similar to those shown before (20 pA, 5 ms, noise at 10% of baseline fluorescence, deblurring at 0.88 μm), but the source diameter varied between 0.2 and 1.5 μm. ● in Fig. 4, B and C, plots peak current and FWHM of the derived release against source diameter. It can be seen that the method evaluates current well at every diameter, but only follows the changes in diameter at values beyond 0.5 μm (C). The spatial dimension of the source is overestimated at diameters below 0.6 μm, an evidence of limited spatial resolution, due to noise and the optical spread of the microscope.

○, in Fig. 4, B and C, illustrates results of applying the algorithm to simulations with noise at 30% of F_0, a level characteristic of individual experimental sparks. Under these conditions, the algorithm can be used provided that fluorescence images are smoothed first, that a more heavily filtering differentiator is used (see methods), and that no deblurring correction is applied. Given the high level of noise, the results change with different noise realizations. Fig. 4, ○, represents averages of six realizations, bars are ±SEM. In this form, which can be applied to individual experimental sparks, the algorithm still evaluates release current within 50% error (B), but fails to report changes in source diameter under 1 μm (C). In summary, the algorithm evaluates release current well under realistic conditions of noise, within a wide range of source parameters. It is able to detect changes in source diameter above 0.7 or 0.8 μm when used with averages, or above 1 μm when used with individual sparks.

The Release Current of Experimental Sparks

The characteristics of sparks obtained with two different experimental techniques were somewhat different.

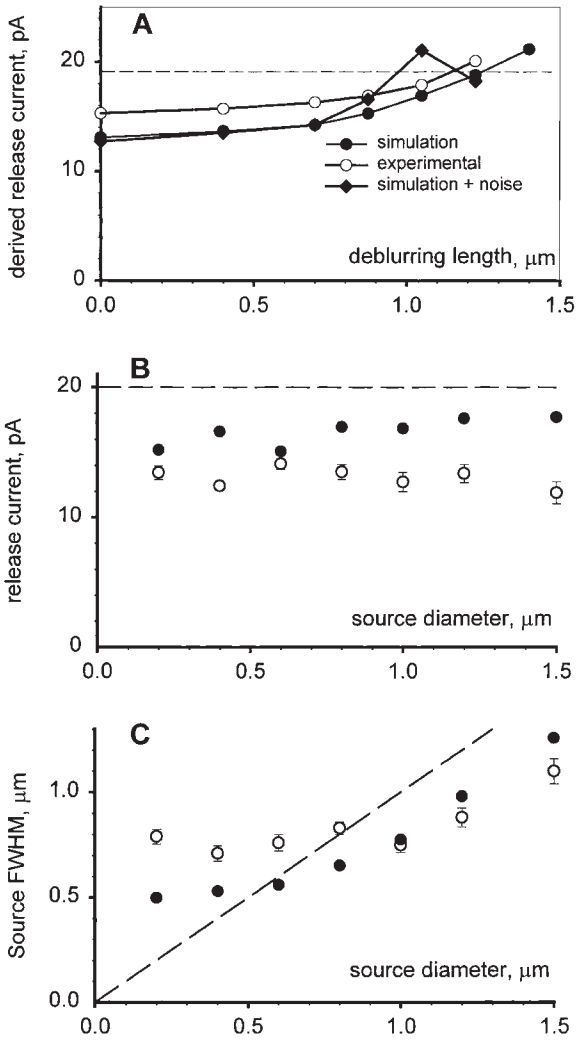

Figure 4. The consequences of deblurring and varying source diameter. (A) Peak of derived release current versus "deblurring length," the $FWHM_z$ of the PSF used for deblurring, which ranges from 0 (no correction) to 1.4 μm (full correction). $FWHM_{xy}$ was equal to $FWHM_z/3.5$. Filled symbols: simulations for a source as in Fig. 2 with (◆) or without noise at 10% of F_0 (same as in Fig. 3). Open circles: results for an average of 157 experimental sparks illustrated in Figs. 5 and 6. Note that the dependence of the current estimate is monotonic and smooth for simulations without noise (●), but goes through a peak or an abrupt change in slope for the experimental average and simulations with noise, at or about a deblurring length of 0.9 μm. (B) Peak of derived release current and (C) FWHM versus source diameter, for simulations of sparks with a 20 pA/5 ms current from a source of variable diameter. Filled symbols: simulations with noise added at 10% of F_0. The analysis was carried out as it is done with spark averages (see text). Open symbols: simulations with noise added at 30% of F_0. The analysis was as done with individual sparks (see text). Represented are averages ± SEM for six realizations of pseudorandom noise. Note a good agreement between the low noise estimates and the simulation current (dashed line).

Cells under voltage clamp. Fig. 5 A contains a line scan image obtained from a fiber under voltage clamp, which had been exposed for 45 min to an internal solution with a nominal free $[Ca^{2+}]$ of 100 nM and 610 μM $[Mg^{2+}]$. In all experiments prepared this way, almost no sparks were observed at rest, but small pulse depolarizations elicited many, as illustrated. The plot at bottom represents the relative fluorescence averaged in a 0.43-μm wide region at the position marked by the line a–a′ in Fig. 5 A. The large spark there peaked at 6.0× the resting fluorescence ($\Delta F/F_0 = 5.0$). Under voltage clamp, repeated depolarizations can be applied and large numbers of sparks collected in a short period of time within a small region of the fiber. We illustrate below the application of the release algorithm to an average of such sparks.

The average was made with the events identified and measured by an automatic routine (Cheng et al., 1999) in Fig. 5 A and in nine other images obtained during a brief period. A total of 301 sparks were identified whose amplitude was >1.0 U resting fluorescence. Their morphology is illustrated in Fig. 5, B and C, which plot, respectively, FWHM and rise time versus spark amplitude. The events of amplitude >2.0 U are marked with circles in A and identified with ○ in the scatter plots.

The graphs demonstrate several aspects of spark morphology that were similar in five experiments studied in the same detail (listed in Table II). Events span a wide range of amplitudes, between seven and the limit of detection. There does not seem to be any discrete segregation in morphology among sparks; that is, no systematic difference appears between the morphological parameters of large versus small amplitude sparks. Accordingly, the correlation between amplitude and the other variables is weak or nonexistent. The lines represent first order regressions to the open symbols. The regression coefficient r^2 was 0.102 for the spark width (range 0.012–0.127 in six experiments) and 0.008 (0.000–0.017) for the rise time. This low correlation suggests that the observed spread in amplitude was not a consequence of the existence of multiple spatially resolved sources, which could collectively generate a large spark (such as those described in cardiac muscle by Parker et al., 1996, or Blatter et al., 1997), nor was it the trivial result of exceptionally long rise times in the largest sparks.

The amplitude with which a spark is recorded in a line scan depends on the actual (object) amplitude of the spark and on its position relative to the scanned line, reaching a maximum (image) amplitude when it is centered on the scanned line. Events that appear large in a line scan image are likely to be closer to the scanned line, hence more suitable to our release analysis (which assumes centered sparks). Of course, sparks

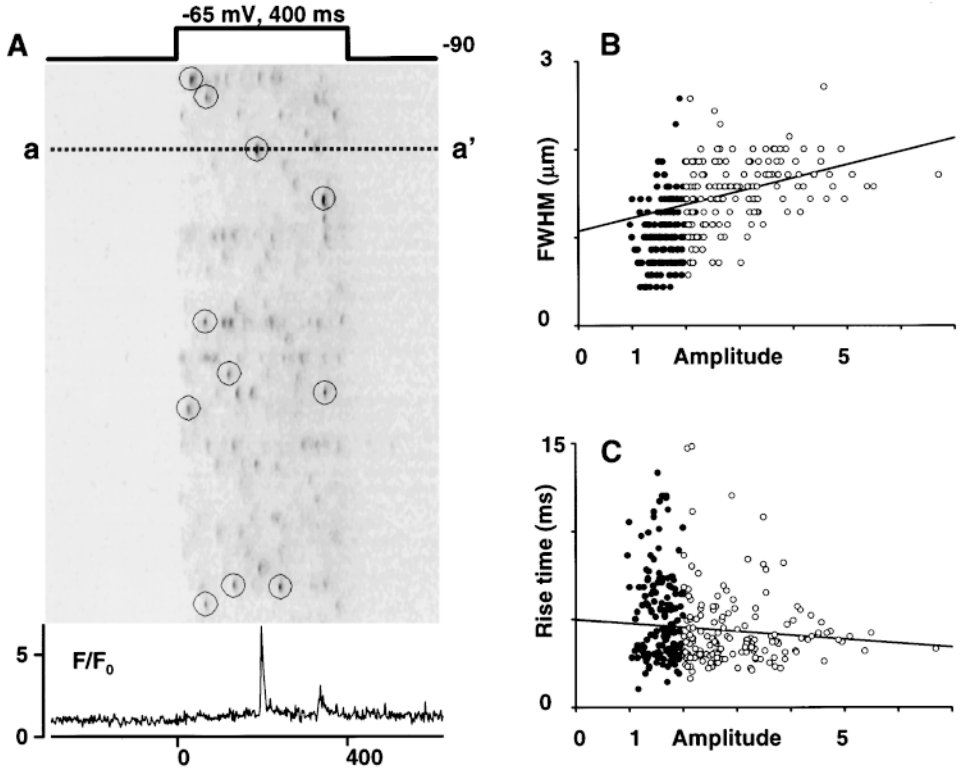

Figure 5. Sparks in a voltage clamped cell. (A) Line scan image of fluorescence [$F(x,t)$]. A pulse to −65 mV was applied as indicated. Fluorescence normalized to its resting value $F_0(x)$, obtained by averaging $F(x,t)$ over the time before application of the pulse. The fluorescence averaged in a 0.43-μm region (three pixels) along line a–a′ is plotted at bottom. (B and C) Spark width (FWHM) and rise time versus peak amplitude, for all sparks in this and nine other images obtained over 12 min within a restricted region of the same fiber. 301 sparks were detected automatically (methods) by the criterion amplitude > 1. The sparks of amplitude > 2, a total of 157 in the nine images, are circled in A and represented by ○ in B and C. Lines represent first order regressions through the latter group. Fiber 0608c, images 26–35.

that are larger as objects are also likely to appear larger in line scans. In the following, we present the results of the release analysis applied to the average of the 157 events with amplitude >2.0 identified in the experiment illustrated. For the considerations above, this average selects a subset of events that are larger as objects and/or originated closer to the scan line.

The application of the release algorithm to the average spark is illustrated in Fig. 6. Parameter values are listed in Table I; $[Mg^{2+}]$ and $[Ca^{2+}]$ were assumed to have the nominal internal solution values. The dye concentration was set at the average of the estimates for each event (which ranged between 38 and 42 μM). The average was centered at the peaks of the sparks and is shown in Fig. 6 A. Because of the low level of noise in the average, no smoothing or other filtering was applied. Partial deblurring was used with deblurring length = 0.88 μm; results with other degrees of deblurring are represented in Fig. 4 A, ○. The release flux density calculated by the algorithm is represented in Fig. 6, B–E. The derived release current is plotted in F.

The algorithm applied to this average spark results in flux that arises from a region 0.5 μm wide, and has a half magnitude duration of 6.3 ms and an amplitude of 16.9 pA. It is demonstrated later that duration and width are quite insensitive to assumptions in the method. The calculated current, however, depends steeply on $[Ca^{2+}]_0$. When, instead of 100 nM (the concentration set in the cut-end solutions), $[Ca^{2+}]_0$ was assumed to be 50 nM, peak current was reduced by ~35% (Fig. 6 F). The dependence is explicable because [fluo-3] is derived from resting fluorescence, which is approximately proportional to both [fluo-3] and $[Ca^{2+}]_0$, hence a change in assumed $[Ca^{2+}]_0$ alters [fluo-3] and the derivation of $[Ca^{2+}](x,t)$.

In every fiber prepared the same way, several hundred sparks were identified (100 or more of which were

TABLE II

Average Morphology of Sparks Under Voltage Clamp

Fiber	Events	Amplitude	FWHM	FDHM	Rise time
			μM	*ms*	*ms*
0414a	100	2.88	1.44	11.2	4.64
0414b	157	2.86	1.35	9.80	3.80
0507b	103	2.96	1.48	11.0	5.52
0608c	157	2.99	1.52	9.83	4.31
0619a	230	2.96	1.50	10.3	4.55
Average	149	2.93	1.46	10.4	4.56
SEM	16.0	0.03	0.04	0.37	0.36

Sparks selected automatically as described in methods by the criterion (amplitude ≥2.0). 5–10 line scan images, obtained while the fiber was pulsed to between −66 and −62 mV, were processed per experiment. The records were not filtered or corrected for blurring. The second column gives the number of identified events. Amplitude of the event was calculated on the normalized fluorescence, as the difference between maximum and local average before the event, on a spline interpolate of the time dependence at the center of the spark. FDHM was calculated on the same interpolate. dye_T was calculated at between 32 and 87 μM.

>2.0 in amplitude). The average morphological parameters, listed in Table II, and the calculated dye_T, were very similar in all cases, hence the release must have been similar.

Permeabilized fibers. It was possible to reduce the uncertainty in the derivations by using the permeabilized fiber preparation, described in methods, in which the fiber membrane is cut at multiple locations and the cell is immersed in the internal solution. Intracellular fluorescence increases with a time constant of 10–20 min. For analysis of these experiments, it is assumed that free [Ca^{2+}] has the value present in the internal solution (an assumption consistent with model simulations of Uttenweiler et al., 1998). dye_T is derived from the internal resting fluorescence as described in methods. Sparks occur spontaneously in this preparation, and their frequency can be controlled by varying free [Mg^{2+}] (Lacampagne et al., 1998). A line scan image of a permeabilized fiber is in Fig. 7. Shown is the fluorescence normalized to its resting value $F_0(x)$. This image is representative of several experiments in which dye_T reached a value close to 400 μM (that is, F_0 reached a value close to that in the 200 μM dye internal solution in which the fiber was immersed).

Unlike the situation with voltage-clamped fibers, the sparks obtained with permeabilized fibers were fewer and did not allow for massive averaging. Limited averaging could be done occasionally, as in the case of Fig. 7. The image shows several sparks arising at the same triad in a field that was of very low activity elsewhere. Therefore, it is likely that all those sparks were generated at the same release unit (Klein et al., 1999). The fluorescence profile in a 0.39-μm region along Fig. 7, a–a′, plotted at bottom, reveals seven sparks whose morphological parameters are represented in B and C. Note the brevity of rise times, of 4 ms or less, their poor correlation with amplitude (regression line plotted in Fig. 7 C, $r^2 = 0.074$), and their large width, close to 2 μm for all but the smallest event. These seven sparks, unusual for originating at the same spot, are not unlike other large sparks observed in permeabilized fibers. Compared with the events under voltage clamp (whose average parameter values are in Table II), large sparks in permeabilized fibers were often wider, briefer, and of shorter rise times. A detailed comparison of events under different conditions is currently in progress (G. Pizarro, A. González, W.G. Kirsch, N. Shirokova, and E. Ríos, manuscript in preparation).

Fig. 8 illustrates the application of the release algorithm to an average of the four largest sparks in Fig. 7. No deblurring was used. The parameter values were the same as in the previous case, except for [Mg^{2+}], which was set to the concentration applied, 0.15 mM. Fig. 8 A represents the spark average, after smoothing, and B–E represent the calculated release flux density. The current (F) peaked at 15.8. Half width of the release source was 1.1 μm and half duration was 7.3 ms.

Release was calculated in the same way for large sparks in 16 images from 12 similarly prepared fibers. The results are listed in Table III. The average parameters of the release source include a current of 14.4 pA, duration of 7.5 ms, and half width of 0.89 μm.

Uncertainties in the Calculation of Release Flux

As illustrated above, the algorithm produces adequate estimates of release current when applied to sparks that are generated by the same process modeled in the algorithm and using the same parameter values. Neither condition applies with real data; there may be differences in parameter values, or other differences (for instance lumped components, diffusion barriers, etc., not considered in the present homogeneously distributed model of removal).

As a way to gauge the likely range of the first class of errors, we imposed parameter changes in the calculation of release for the average of 157 sparks studied in Fig. 6. The changes and the resulting morphological measures of derived release current are listed in Table IV. Changes in parameters were introduced one at a time. For those parameters expected to have a major effect, two alternative values were used, defining a reasonable range that should comprise the actual fiber values. This was done for the diffusion coefficients of Ca^{2+}, the dye, and ATP, and for the concentrations of ATP, EGTA, and Mg^{2+}. For maximum pump rate and the concentrations of troponin and parvalbumin sites, only one change was explored, sufficient to demonstrate a relative lack of consequences.

Changing properties of the dye:Ca^{2+} reaction had the greatest effects. When the ON rate constant was reduced by a factor of 2.5, to bring K'_d to the upper value in the range estimated in vivo by Harkins et al. (1993), the derived release current increased by ~50% (because the change increased the estimated Ca^{2+} concentration transient). Similar changes in current were produced by increasing threefold the dye diffusion coefficient. Because the model considers multiple removal processes, even drastically changing one removal parameter alone had little effect. The only substantial change in the estimate of current (increase by ~50%), occurred when the concentration of EGTA was increased fivefold. The spatial and temporal characteristics of the derived release source were even more robust. Other than changing the properties of the dye, the only changes with major consequences on the derived release width and duration were large changes in [ATP] and the reduction of [Mg^{2+}] to 0.15 μM (which increases the free concentrations of ATP and parvalbumin). Changes in troponin and the SR pump had little effect on the release estimate.

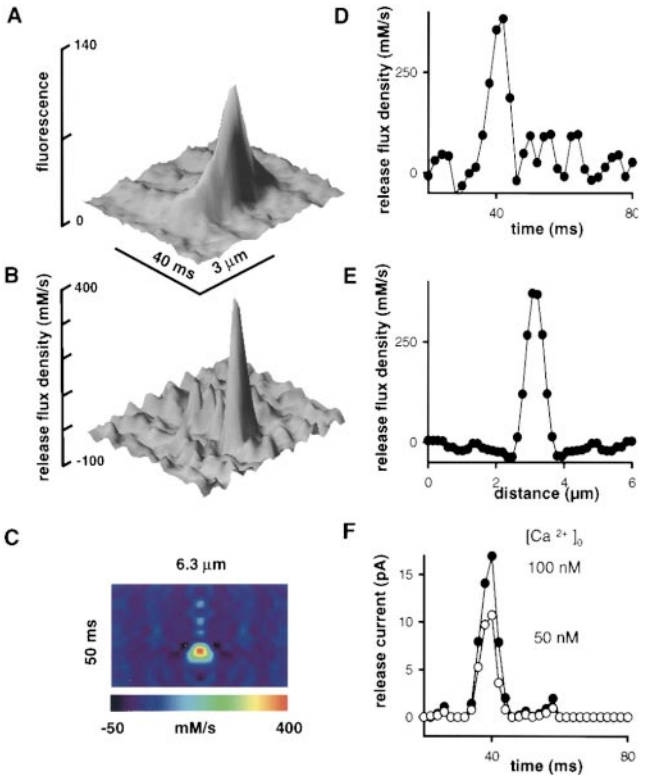

Figure 6. Release analysis of sparks elicited in a voltage clamped cell. (A) Average of 157 sparks of amplitude > 2, in the experiment of Fig. 5. (B and C) Representations of the release flux density, calculated with the parameters of Table I, after deblurring (with $FWHM_{xy} = 0.25$ μm and $FWHM_z = 0.88$ μm). (D) Temporal and (E) spatial cuts of the calculated release flux through its center. (F) Release current, calculated with two different assumptions for resting $[Ca^{2+}]$.

To elicit a "low estimate" of release current, the method was applied with all buffer concentrations reduced threefold. The derived release parameters are in the last row of Table IV. With such low values, the release current was 8.05 pA.

A minimum estimate of another sort was reached by simply integrating the dye-binding term ($\partial[dye{:}Ca^{2+}]/\partial t$) in the representation of flux density given by Eq. 4. The meaning of this estimate is illustrated in Fig. 9, where it is developed for both the average of four sparks in Fig. 8 and a simulated spark copying the experimental conditions. Fig. 9, top, shows the concentration of $dye{:}Ca^{2+}$, which for the experimental spark is calculated from the fluorescence following Eq. 1. Fig. 9, middle, shows the rate of change of $[dye{:}Ca^{2+}]$, which in both cases reaches a pronounced maximum right before the peak of fluorescence. The bottom graphs plot this rate of change ($\partial[dye{:}Ca^{2+}]/\partial t$) at the time of its maximum, versus x. Intuitively, the Ca^{2+} release flux at this time should be greater than the total flux of Ca^{2+} binding to the dye, which can be calculated by volume integration of the rate of change shown. The result of the volume integration, expressed as a current intensity, is plotted in the bottom graphs as a function of position, starting from zero at the center of the spark. The limiting value, reached far from the spark center, is ~15 pA (0.074 fmol/s) in the experimental case. The simulated spark reaches a similar maximum rate of change, but has lesser spatial spread. Accordingly, the total flux binding to the dye in the simulation corresponds to <4 pA. In every case tested, the integrated rate at early times during a spark was less than the maximum release flux, in agreement with the idea that the other removal and diffusion processes are largely positive at these early times. The value of this dye-related estimate is listed for all events analyzed in permeabilized fibers, in the last column of Table III. Its average is 8.26 pA.

Different microscope objectives. To test the possibility that release evaluations were affected by the less than ideal axial resolution determined in our conditions, we compared the spark morphology and release flux with our preferred C-apochromat objective and the 63×, 1.4 N.A., oil immersion plan-apochromat (the PSFs of both objectives are compared in methods). Pooled averages and their standard errors, for 1,850 sparks obtained with the C-apochromat and 1,591 in five experiments in which the system was aligned and all images were acquired with the plan-apochromat were, respectively: amplitude, 1.09 (0.04) and 1.10 (0.05); FWHM (μm), 1.40 (0.07) and 1.57 (0.09); FDHM (ms), 9.10 (0.4) and 9.87 (0.4). None of these differences were significant. (The average amplitudes were smaller than in Table II due to the use of a lower detection criterion.) In one experiment, the system was aligned and initial images were acquired with the C-apochromat, and then the fiber was imaged with the plan-apochromat and additional images were acquired. Again, no significant differences were observed between averages of 239 and 198 events obtained with the two objectives. Because sparks were similar, the release algorithm applied to the largest sparks or to spark averages gave similar results in both types of experiments with either objective. The conclusion is that the better axial resolution provided by the oil-immersion objective does not result in a spark of greater amplitude, which may be an indication of differences in the PSF that require more than the FWHM for their description. We continue to prefer the water immersion C-apochromat because the morphology of events imaged with it does not appear to depend on depth within the cell, which allows one to obtain many more images from the same fiber.

discussion

An algorithm introduced for the evaluation of release flux in cardiac Ca^{2+} sparks (Blatter et al., 1997) was modified and applied to sparks of skeletal muscle. The

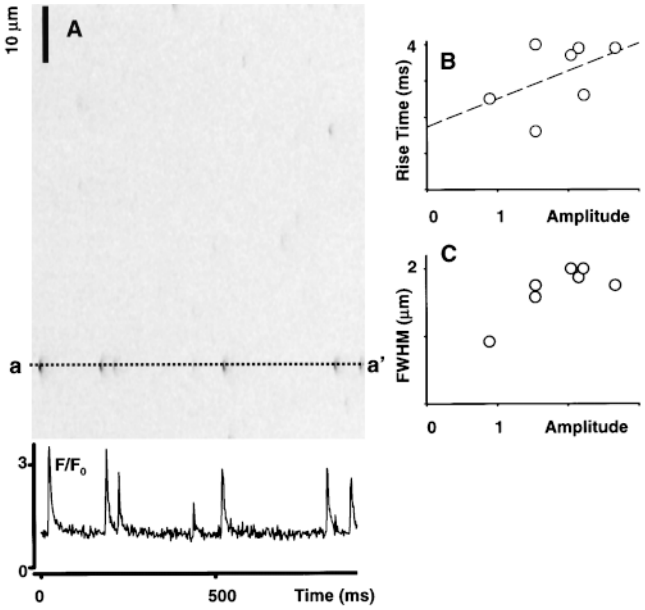

Figure 7. Sparks in a permeabilized cell. The fiber was permeabilized by notches and exposed for 45 min to an internal solution with 0.15 mM free Mg^{2+} and 200 μM fluo-3. (A) Line scan image of fluorescence normalized to F_0. Bottom, normalized fluorescence, averaged over a 0.39-μm–wide region along the line a–a′. (B and C) Morphology of the events at position a–a′. Note the brevity of rise times, of 4 ms or less, their poor correlation with amplitude (regression line plotted in B, $r^2 = 0.074$), and their large width, close to 2 μm for all but the smallest event. Experiment 0812c, image 22.

algorithm yields release flux density ($\dot{R}$, a function of space and time), which can then be integrated to obtain total flux (or current).

Evaluation of the Algorithm

We first tested the consistency of the algorithm (or "backward" calculation) on sparks simulated as the result of Ca^{2+} diffusion from a finite source (the "forward" calculation). The backward calculation retrieved approximately the same total current used in the forward construction, over a wide range of release current. There were some deviations, namely the flux density in the backward calculation was ~55–60% of that in the simulation, and the half width of the region where the back-calculated source resided was slightly greater than the simulation source. These errors appear to be due to the finite spatial and temporal resolution of the experimental methods, which requires discrete and necessarily coarse approximations to steeply space- and time-dependent variables. They approximately compensated each other, however, resulting in a nearly correct determination of total current.

A set of more realistic tests, which characterized the performance and limitations of the method when applied to experimental data, included noise in the

table iii

Release Calculation Algorithm Applied to Different Images from Permeabilized Fibers

Image	Spark amplitude	dye_T	Peak flux density	Release			
				Current	FWHM	FDHM	Dye term
		μM	mM/s	pA	μm	ms	pA
812a2	1.9	377	154	14.7	0.55	8.5	10.8
812b7	1.5	256	81	16.6	0.90	6.1	3.19
812c12*	2.2	356	92	15.8	1.10	7.3	14.8
812d13	2.1	328	114	14.6	0.93	4.6	11.0
813a2	1.7	339	91	13.9	0.96	6.9	8.40
813a6	2.8	325	88	20.7	1.18	6.7	14.4
813b1	2.7	235	154	18.1	0.81	6.7	7.84
817a76	1.8	184	83	11.9	1.00	8.6	5.74
817a76	2.2	184	112	17.0	0.83	8.4	2.84
817b10	1.9	170	185	7.4	0.69	9.8	4.74
817b12	2.2	177	152	14.2	0.54	8.8	8.96
819c22	2.9	169	176	15.3	0.76	8.8	2.69
819c22	2.7	166	146	14.1	0.86	8.1	4.04
819c28	2.5	161	145	12.3	0.77	7.6	6.49
820b20	1.6	230	96	15.3	1.11	6.9	3.49
824a45	1.3	211	112	5.0	0.57	6.4	3.55
Average	2.14	260	119	14.4	0.89	7.5	8.28
SEM	0.10	19.0	7.8	0.81	0.05	0.27	1.07

The first number and letter in column 1 identify the experiment, the last number in column 1 identifies the image. Repeated numbers identify sparks from the same image. *Average of four sparks, represented in Figs. 8 and 9. Column 2 lists amplitude of the event, calculated as in Table II. dye_T was calculated using Eq. 2. Current, FWHM, and FDHM were calculated on the release flux waveform, derived after smoothing and without deblurring. The last column lists the dye-related estimate of release current illustrated in Fig. 9.

records. Because Ca^{2+} removal and the monitoring dye reaction are mass action-driven processes that occur at finite rates, the release algorithm involves differentiation stages that increase noise. Additionally, it starts with a deblurring step, to undo the blurring introduced by imaging. Deblurring is basically a deconvolution resulting in a greater enhancement of the high (spatial) frequency components of the signal, and a disproportionate increase in noise when applied to real data.

To counter these problems, we altered the method in two ways, we used less than full deblurring (that is, deblurring for a sharper PSF than actually measured) and we used smoothing and filtering digital differentiation. The effects of changing the deblurring length (FWHM of the PSF assumed in the correction) was explored on simulated sparks. This study, illustrated in Fig. 4, shows that increasing the deblurring length gradually increases the estimate of release current. The change is gradual, albeit sizable (in going from no deblurring to full deblurring the current estimate may increase by as much as 40%). In the same tests, noise, added to the simulations at the levels found in spark averages, results

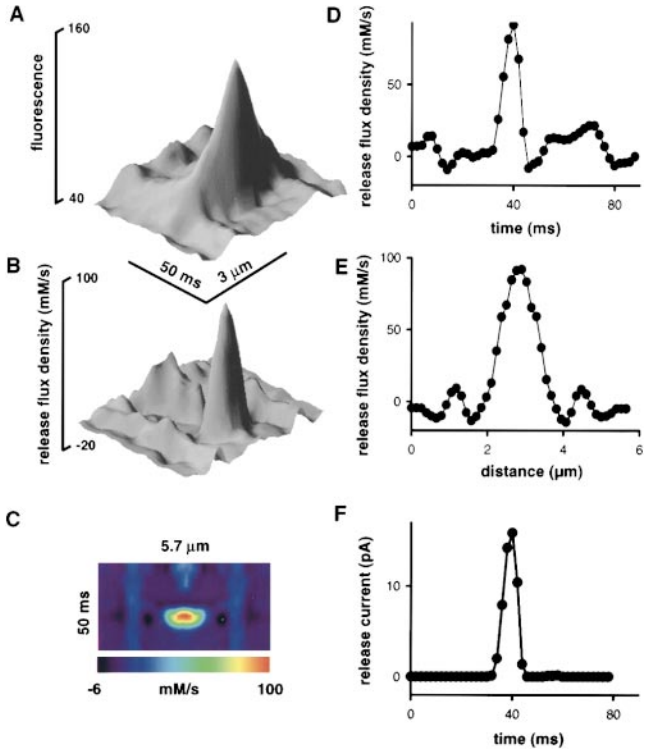

Figure 8. Release analysis of sparks elicited in a permeabilized cell. (A) Fluorescence spark, obtained by averaging the four largest sparks in Fig. 7, smoothed. (B and C) Multidimensional representations of the release flux density, derived with the parameters of Table I, using procedures that are adequate for individual events (smoothing and filtering differentiation, no deblurring). (D) Temporal and (E) spatial cuts of the derived release flux. (F) Release current obtained by volume integration of the central peak of release flux at different times.

in an erratic morphology of derived release beyond a certain point. This translates to a limiting value of ~0.9 μm for the deblurring length.

Using this practical level of deblurring correction, we then asked how would the algorithm depend on the spatial aspects of the source, namely the diameter (because the source is assumed to be spheric). As shown in Fig. 4, the algorithm underestimated source current by ~30%, regardless of source diameter. The source radius reported by the algorithm was rather insensitive to changes in actual source geometry below 0.7 μm. This limits the ability of the technique to distinguish between extended and point sources.

In summary, the algorithm slightly underestimates source current, slightly overestimates source duration, and reflects source diameter beyond ~0.7 μm. Its performance is degraded when used with digital low-pass filtering, but release current is never overestimated.

Applications to Experimental Sparks

The method was applied to an average including every spark of amplitude above 2 F_0 obtained under voltage clamp in the same cell. Because the images were acquired over a short period, the dye concentration varied <10%, which makes it legitimate to average the events and then process the average. There was a poor correlation between amplitude and rise time for these sparks, as well as a low positive correlation between amplitude and half width. This suggests that the selected sparks were not "special", other than by surpassing the amplitude criterion. Their large amplitude indicates that the sparks originated near the scanning line, were large as objects (i.e., before imaging), or both.

The derived source current is represented in Fig. 4 (○) for various values of deblurring length. Comparing with the values obtained with simulations, it appears that the average spark originated from a source of at least 20 pA (the release current in the simulation). The range of source widths derived for the average spark, 0.47–0.7 μm, does not allow one to tell whether the flux originated at a point or an extended source.

The algorithm was also applied to sparks from permeabilized fibers immersed in internal solution. This technique had two advantages. Dye concentrations in the few hundred micromolar were achieved rapidly inside the cells, leading to a more robust determination of release flux. An even more important advantage of the permeabilized preparation was the better determination of resting [Ca^{2+}], which should have been close to that in the equilibrating internal solution. The method was applied to individual events or to averages of just a few, which typically required low-pass filtering of the images and did not allow for deblurring.

For 19 large sparks from 11 permeabilized cells, the average release current was 14.4 pA, and half width 0.89 μm. Considering the conditions under which the algorithm was applied, the release current is probably an underestimate, and therefore not inconsistent with the estimate of 20 pA obtained under voltage clamp.

The large source width derived under these conditions should not be overinterpreted because the algorithm applied to simulations with high noise levels was quite insensitive to source width in the range below 1 μm. Nevertheless, it is interesting that in several experiments source diameters >1 μm were derived. In all those cases, fluorescence sparks had large width. One way in which sparks of such width could be simulated in forward calculations was by assuming source diameters >1 μm. These observations therefore raise the possibility that some wide sparks of high amplitude may originate from sources of resolvable size. One problem with this interpretation is that scanning was perpendicular to the Z disks (and the long axis of the transverse tubules), hence it is difficult to imagine a structural substrate for such extended release sources. The large width of some sparks therefore remains without a convincing explanation or simulation.

table iv

Effect of Parameter Changes on Release Current Derived by the Algorithm

Parameter changed	From	To	Release Current	Release FWHM	Release FDHM
			pA	*μm*	*ms*
None (reference	—	—	16.9	0.497	6.3
D_{Ca}	3.5×10^{-6} cm^2 s^{-1}	7×10^{-6} cm^2 s^{-1}	19.6	0.497	5.6
		1.75×10^{-6} cm^2 s^{-1}	15.7	0.680	6.6
D_{dye}	2×10^{-7} cm^2 s^{-1}	6×10^{-7} cm^2 s^{-1}	26.9	0.512	5.9
		1×10^{-7} cm^2 s^{-1}	18.3	0.694	6.6
D_{ATP}	1.4×10^{-6} cm^2 s^{-1}	2.8×10^{-6} cm^2 s^{-1}	20.6	0.511	5.7
		0.7×10^{-6} cm^2 s^{-1}	15.2	0.680	6.6
[ATP]	5 mM	1 mM	19.5	0.877	7.1
		10 mM	19.0	0.480	5.8
$k_{ON\ Ca:dye}$	3.2×10^8 M^{-1} s^{-1}	1.3×10^8 M^{-1} s^{-1}	26.9	0.482	5.5
Max. pump rate	9.8 mM s^{-1}	2 mM s^{-1}	16.1	0.497	6.3
[Troponin]	0.24 mM	0.04 mM	16.0	0.497	6.3
[Parvalbumin]	1 mM	0 mM	15.4	0.497	6.2
[EGTA]	1 mM	5 mM	24.8	0.709	6.3
		0 mM	13.7	0.629	7.9
[Mg^{2+}]	0.61 mM	0.15 mM	20.8	0.475	5.7
All buffers*			8.05	0.497	5.2

The release calculation algorithm, including deblurring (with $FWHM_y$ = 0.25 μm and $FWHM_z$ = 0.88 μm), was applied to the average of 157 sparks illustrated in Figs. 6 and 7. The same spark average was analyzed with standard parameter values in Fig. 4 (○). One parameter was changed at a time, as listed in column 1. The parameter's reference value is listed in the second column and the changed value in the third. The last three columns give the morphology of the release waveform derived by the algorithm. *Concentration of all buffers (ATP, EGTA, pump sites, troponin, and parvalbumin) changed to one third of reference.

Estimates of Release Current and Their Implications

The present estimates of release current underlying a spark should be compared with single channel currents recorded in bilayers, in conditions as close as possible to physiological. Mejía-Alvarez et al. (1988) studied heavy SR cardiac release channels carrying Ca^{2+} current in the lumenal-to-cytoplasmic direction, driven by gradients of 2–10 mM, and in the presence of high concentrations of Cs^+ (as a substitute for the inhibitory effects of K^+ on Ca^{2+} current). At 2 mM lumenal Ca^{2+} (similar to $[Ca^{2+}]_{SR}$ values determined in cardiac muscle by Chen et al., 1996), and in the presence of symmetric 150 mM Cs^+, the single channel current was 0.35 pA. This is not the best possible representation of the physiological situation because Mg^{2+} was not included. It is, however, a good representation of our permeabilized fibers, in which $[Mg^{2+}]$ was 0.15 mM.

The comparison implies that ~60 fully open channels are necessary to account for release in the sparks studied here. This number, however, is subject to multiple possible errors in parameter values or in the structure of the model itself. For this reason, we provide two lower estimates of current. One is 8.09 pA, obtained when concentrations of all the removal molecules of the muscle cell model were reduced to one third their consensus values. Another low estimate, not requiring any assumptions about removal processes, was obtained by computing the rate of change of dye-bound Ca^{2+} before the fluorescence peak. This estimate is equivalent to the rate of change of "signal mass," defined by Sun et al. (1998) to evaluate Ca^{2+} release underlying $InsP_3$-triggered signals in *Xenopus* oocytes. Its average for the large sparks of Table III is 8.28 pA. Using these low estimates, 20 or 25 channels are required to account for the release current.

The unitary current could be greater if $[Ca^{2+}]_{SR}$ was higher than the 2 mM used in the bilayer experiments. The range of possible values of $[Ca^{2+}]_{SR}$ is limited, however. In cardiac muscle, $[Ca^{2+}]_{SR}$ has been found to vary within a narrow band (Chen et al., 1998), about a decade lower than its thermodynamic limit of 10–20 mM. This agrees with evidence that the SR pump stops working, for kinetic rather than thermodynamic reasons, at a $[Ca^{2+}]_{SR}$ of ~5 mM (Inesi, 1994). Assuming 5 mM as the maximum possible concentration would increase at most by a factor of 2.5 the single channel current, resulting in a lower limit of eight for the number of channels simultaneously open during the rise time of a large spark.

Three recent reviews (Shirokova et al., 1998; Cannell and Soeller, 1999; Schneider, 1999) consider the question of number of channels underlying a spark. Sparks were originally proposed to arise from one or a few

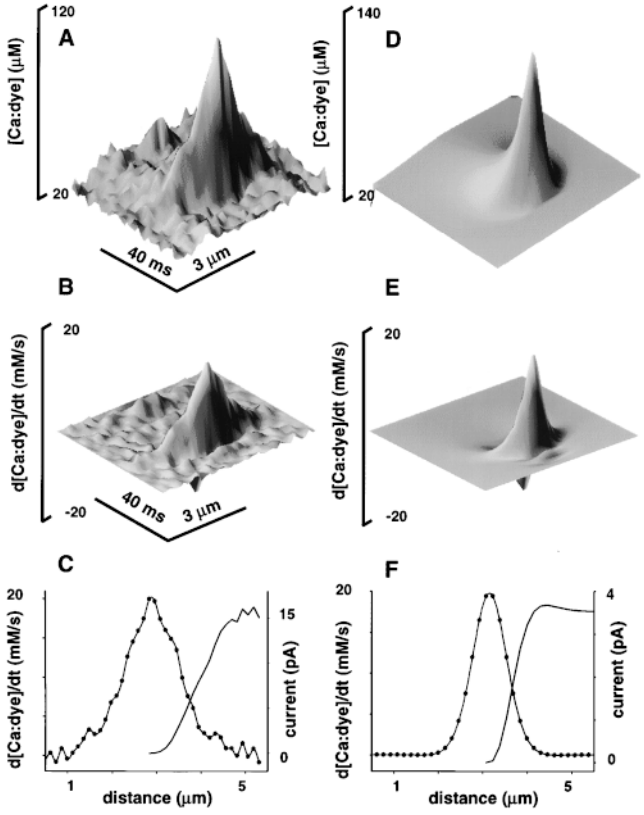

Figure 9. The dye-binding term of release flux. (A) The concentration of dye:Ca^{2+}, derived (by Eq. 1) from the fluorescence average of four sparks illustrated in Fig. 8. (B) $\partial[dye{:}Ca^{2+}]/\partial t$, derived by partial differentiation of A. (C) Symbols, $\partial[dye{:}Ca^{2+}](x,t_{max})/\partial t$ at the time of its maximum(t_{max}), as a function of x. Line, volume integral of $\partial[dye{:}Ca^{2+}]/\partial t$ at the time of its maximum. The integral was computed as

$$4\pi\int_{x_0}^{x}\partial[dye{:}Ca^{2+}](u,t_{max})/\partial t\,(u-x_0)^2\,du,$$

where x_0 is the central value of x, and converted to Ca^{2+} current. (D) [dye:Ca^{2+}] in a simulation imitating the experimental spark (20 pA, 6 ms, dye_T = 350 μM, other parameter values in Table I). (E) $\partial dye{:}Ca^{2+}]/\partial t$ in the simulation. (F) $\partial[dye{:}Ca^{2+}]/\partial t$ at the time of its maximum, and its volume integral expressed as a current. Note that the current reaches an approximately fourfold greater value for the experimental spark, even though the maximum rates are approximately equal. This is due to an ~50% greater spatial spread of the experimental spark.

channels in cardiac muscle (Cheng et al., 1993), and one (Tsugorka et al., 1995) or "one or two" (Klein et al., 1996) in skeletal muscle. Evidence for a many-channel mechanism has increased with the observation of release in events smaller than sparks (Bhat et al., 1987; Lipp and Niggli, 1996, 1998; Shirokova and Ríos, 1996, 1997) and of multifocal sparks (Parker et al., 1996; Blatter et al., 1997). Similarly, it is believed that "calcium puffs" produced by release through $InsP_3$ receptors are due to activation of multiple channels (Bootman et al., 1997; Sun et al., 1998). Part of the evidence for one- or two-channel mechanisms was the observation of multiple modes in the distribution of event amplitude (Tsugorka et al., 1995; Klein et al., 1996), but the existence of modes has been contested on the basis of simulations of confocal sampling (Pratusevich and Balke, 1996), and on theoretical grounds (Cheng et al., 1998). In favor of single channel mechanisms, it has been shown that release under a spark starts and ends abruptly (Lacampagne et al., 1999) and that Imperatoxin A, which induces prolonged openings of release channels in bilayers, causes the appearance in muscle fibers of long duration events of sizable amplitude (Shtifman et al., 1999).

In a model of Stern et al. (1997), closely packed arrays of release channels interact for activation and inactivation, by virtue of their sensitivity to Ca^{2+}. These functionally interacting arrays, termed "couplons," correspond structurally to all the release channels on one side of one junctional segment of transverse tubule (Franzini-Armstrong and Jorgensen, 1994). In the simulations of Stern et al. (1997), a couplon can activate rapidly, in full or in part, and then inactivate, to generate an event with properties similar to sparks. The above estimate of 60 channels in a large spark is in reasonable agreement with the number of channels that fit on one side of a junctional unit (the units of largest size, 0.9 μm, Protasi and Franzini Armstrong, personal communication, fit a double row of 60 channels at 30-nm spacing). The minimum estimate of eight channels per spark suggests instead partial couplon activation.

The present conclusions apply to sparks that were selected for their large amplitude. Examination of the amplitude distribution of sparks in view of the artifacts introduced by the process of line scanning (González et al., 1999), indicates that there is a wide, perhaps severalfold range of spark currents. The conclusion that the large sparks studied here require at least eight open channels must therefore be accompanied by the realization that other, smaller sparks of the same fibers must involve fewer simultaneously open channels, perhaps leading to a reconciliation of the different views, as sparks would then be produced by the opening of variable numbers of channels.

We are grateful to Dr. Wolfgang G. Kirsch (Rush University) for suggestions on the manuscript.

This work was supported by grants from the National Institutes of Health (NIH) and the Muscular Dystrophy Association to E. Ríos, by intramural research programs of NIH to M.D. Stern, and a grant from NIH to N. Shirokova. A. González was the recipient of a Senior Fellowship from the American Heart Association of metropolitan Chicago.

Submitted: 13 October 1998 Revised: 7 May 1999 Accepted: 10 May 1999

references

Agard, D.A., Y. Hiraoka, P. Shaw, and J.W. Sedat. 1989. Fluorescence microscopy in three dimensions. *Methods Cell Biol.* 30:353–377.

Baylor, S.M., W.K. Chandler, and M.W. Marshall. 1983. Sarcoplasmic reticulum calcium release in frog skeletal muscle fibres estimated from Arsenazo III calcium transients. *J. Physiol.* 344:625–666.

Baylor, S.M., and S. Hollingworth. 1998. The transient binding of calcium to ATP and diffusion of Ca-ATP help shape the amplitude and time course of the myoplasmic free Ca transient. *Biophys. J.* 74:A235. (Abstr.)

Bhat, M.B., J. Zhao, W. Zang, C.W. Balke, H. Takeshima, W.G. Wier, and J. Ma. 1987. Caffeine-induced release of intracellular Ca^{2+} from Chinese hamster ovary cells expressing skeletal muscle ryanodine receptor. Effects on full-length and carboxyl-terminal portion of Ca^{2+} release channels. *J. Gen. Physiol.* 110:749–762.

Blatter, L.A., J. Hüser, and E. Ríos. 1997. Sarcoplasmic reticulum Ca^{2+} release flux underlying Ca^{2+} sparks in cardiac muscle. *Proc. Natl. Acad. Sci. USA.* 94:4176–4181.

Bootman, M., E. Niggli, M. Berridge, and P. Lipp. 1997. Imaging the hierarchical Ca^{2+} signalling system in cells. *J. Physiol.* 499: 307–314.

Cannell, M.B., and C. Soeller. 1999. Perspective: mechanisms underlying calcium sparks in cardiac muscle. *J. Gen. Physiol.* 113: 373–376.

Chen, W., C. Steenbergen, L.A. Levy, J. Vance, R.E. London, and E. Murphy. 1996. Measurements of free Ca^{2+} on sarcoplasmic reticulum in perfused rabbit heart loaded with 1,2-bis(2-amino-5,6-difluorophenoxy)ethane-N,N,N′,N′-tetraacetic acid by 19F NMR. *J. Biol. Chem.* 271:7398–7403.

Chen, W., R.E. London, E. Murphy, and C. Steenbergen. 1998. Regulation of the Ca^{2+} gradient across the sarcoplasmic reticulum in perfused rabbit heart. A 19F nuclear magnetic resonance study. *Circ. Res.* 83:898–907.

Cheng, H., W.J. Lederer, and M.B. Cannell. 1993. Calcium sparks: elementary events underlying excitation–contraction coupling in heart muscle. *Science.* 262:740–744.

Cheng, H., L.S. Song, N. Shirokova, A. González, E.G. Lakatta, E. Ríos, and M.D. Stern. 1998. Amplitude distribution of calcium sparks in confocal images. Theory and studies with an automatic detection method. *Biophys. J.* 76:606–617.

Franzini-Armstrong, C., and A.O. Jorgensen. 1994. Structure and development of E-C coupling units in skeletal muscle. *Annu. Rev. Physiol.* 56:509–534.

González, A., N. Shiorkova, W.G. Kirsch, G. Pizarro, M.D. Stern, H. Cheng, and E. Ríos. 1999. Size distribution of Ca^{2+} sparks in caffine-stimulated skeletal muscle. *Biophys. J.* 76:A385.

Hamming, R.W. 1989. Digital Filters. Third edition. Prentice Hall, Englewood Cliffs, CA. 189 pp.

Harkins, A.B., N. Kurebayashi, and S.M. Baylor. 1993. Resting myoplasmic free calcium in frog skeletal muscle fibers estimated with fluo-3. *Biophys. J.* 65:865–881.

Inesi, G. 1994. Teaching active transport at the turn of the 21st century. *Biophys. J.* 66:554–560.

Klein, M.G., H. Cheng, L.F. Santana, Y.H. Jiang, W.J. Lederer, and M.F. Schneider. 1996. Two mechanisms of quantized calcium release in skeletal muscle. *Nature.* 379:455–458.

Klein, M.G., A. Lacampagne, and M.F. Schneider. 1999. A repetitive mode of activation of discrete Ca^{2+} release events (Ca^{2+} sparks) in frog skeletal muscle fibers. *J. Physiol.* 515:391–411.

Kushmerick, M.J., and R.J. Podolsky. 1969. Ionic mobility in muscle cells. *Science.* 166:1297–1298.

Lacampagne, A., M.G. Klein, and M.F. Schneider. 1998. Modulation of the frequency of spontaneous sarcoplasmic reticulum Ca^{2+} release events (Ca^{2+} sparks) by myoplasmic [Mg^{2+}] in frog skeletal muscle. *J. Gen. Physiol.* 111:207–224.

Lacampagne, A., C.W. Ward, M.G. Klein, and M.F. Schneider. 1999. Time course of individual voltage-activated Ca^{2+} sparks recorded at ultra-high time resolution in frog skeletal muscle. *J. Gen. Physiol.* 113:187–198.

Lipp, P., and E. Niggli. 1996. A hierarchical concept of cellular and subcellular Ca^{2+} signalling. *Prog. Biophys. Mol. Biol.* 65:265–296.

Lipp, P., and E. Niggli. 1998. Fundamental calcium release events revealed by two-photon excitation photolysis of caged calcium in guinea-pig cardiac myocytes. *J. Physiol.* 508:801–809.

Mejía-Alvarez, R., C. Kettlun, E. Ríos, M.D. Stern, and M. Fill. 1998. Unitary calcium currents trough cardiac ryanodine receptors under physiological conditions. *J. Gen. Physiol.* 113:177–186.

Melzer, W., E. Ríos, and M.F. Schneider. 1984. Time course of calcium release and removal in skeletal muscle fibers. *Biophys. J.* 45: 637–641.

Melzer, W., E. Ríos, and M.F. Schneider. 1987. A general procedure for determining the rate of calcium release from the sarcoplasmic reticulum in skeletal muscle fibers. *Biophys. J.* 51:849–863.

Parker, I., W.J. Zang, and W.G. Wier. 1996. Ca^{2+} sparks involving multiple Ca^{2+} release sites along Z-lines in rat heart cells. *J. Physiol.* 497:31–38.

Pechère, J.F., J.P. Capony, and J. Demaille, 1973. Evolutionary aspects of the structure of muscular parvalbumins. *Syst. Zool.* 22: 533–548.

Pizarro, G., L. Csernoch, I. Uribe, M. Rodríguez, and E. Ríos. 1991. The relationship between Q_γ and Ca release from the sarcoplasmic reticulum in skeletal muscle. *J. Gen. Physiol.* 97:913–947.

Pratusevich, V.R., and C.W. Balke. 1996. Factors shaping the confocal image of the calcium spark in cardiac muscle cells. *Biophys. J.* 71:2942–2957.

Ríos, E., and M.D. Stern. 1997. Calcium in close quarters: microdomain feedback in excitation–contraction coupling and other cell biological phenomena. *Annu. Rev. Biophys. Biomol. Struct.* 26: 47–82.

Sako, Y., A. Sekihata, Y. Yanagisawa, M. Yamamoto, K. Shimada, K. Ozaki, and A. Kusumi. 1997. Comparison of two-photon excitation laser scanning microscopy with UV-confocal laser scanning microscopy in three-dimensional calcium imaging using the fluorescence indicator Indo-1. *J. Microsc.* 185:9–20.

Schneider, M.F. 1999. Perspective: Ca^{2+} sparks in frog skeletal muscle: generation by one, some, or many SR Ca^{2+} release channels? *J. Gen. Physiol.* 113:365–371.

Schneider, M.F., E. Ríos, and W. Melzer. 1987. Determining the rate of calcium release from the sarcoplasmic reticulum in muscle fibers. *Biophys. J.* 51:1005–1007.

Shirokova, N., J. García, and E. Ríos. 1998. Local calcium release in mammalian skeletal muscle. *J. Physiol.* 512:377–384.

Shirokova, N., and E. Ríos. 1996. Activation of Ca^{2+} release by caffeine and voltage in frog skeletal muscle. *J. Physiol.* 493:317–339.

Shirokova, N., and E. Ríos. 1997. Small event Ca^{2+} release: a probable precursor of Ca^{2+} sparks in frog skeletal muscle. *J. Physiol.* 502:3–11.

Shtifman, A., C.W. Ward, H.H. Valdivia, and M.F. Schneider. 1999. Induction of long duration Ca^{2+} release events by Imperatoxin A in frog skeletal muscle. *Biophys. J.* 76:A465. (Abstr.)

Smith, G.D., J.E. Keizer, J.D. Stern, W.J. Lederer, and H. Cheng. 1998. A simple numerical model of calcium spark formation and detection in cardiac myocytes. *Biophys. J.* 75:15–32.

Smith, P.D., G.W. Liesegang, R.L. Berger, G. Czerlinski, and R.J. Podolsky. 1984. A stopped-flow investigation of calcium ion bind-

ing by ethylene glycol bis(β-aminoethylether)-*N*,*N*′-tetraacetic acid. *Anal Biochem.* 143:188–195.

Stern, M.D., G. Pizarro, and E. Ríos. 1997. Local control model of excitation–contraction coupling in skeletal muscle. *J. Gen. Physiol.* 110:415–440.

Sun, X.P., N. Callamaras, J.S. Marchant, and I. Parker. 1998. A continuum of InsP3-mediated elementary Ca^{2+} signalling events in *Xenopus* oocytes. *J. Physiol.* 509:67–80.

Tsugorka, A., E. Ríos, and L.A. Blatter. 1995. Imaging elementary events of calcium release in skeletal muscle cells. *Science.* 269: 1723–1726.

Uttenweiler, D., C. Weber, and R.H. Fink. 1998. Mathematical modeling and fluorescence imaging to study the Ca^{2+} turnover in skinned muscle fibers. *Biophys. J.* 74:1640–1653.

Wilson, T. 1995. The role of the pinhole in confocal imaging system. *In* Handbook of Biological Confocal Microscopy. J.B. Pawley, editor. Plenum Publishing Corp., New York. 167–182.